A New Family of Near-Zero Parasitic Shift Remote Center of Motion Flexure-based Pivots

Célestin Vallat[1]
Micromechanical and Horological Design Laboratory (Instant-Lab),
Department of Mechanical Engineering,
École Polytechnique Fédérale de Lausanne,
Rue de la Maladière 71c, 2000 Neuchâtel
email: celestin.vallat@epfl.ch

Simon Henein
Micromechanical and Horlogical Design Laboratory (Instant-Lab),
Department of Mechanical Engineering,
École Polytechnique Fédérale de Lausanne,
Rue de la Maladière 71c, 2000 Neuchâtel
email: simon.henein@epfl.ch

Remote Center of Motion (RCM) pivots mechanisms are 1-DOF pivots whose axis of rotation is located outside of the physical structure of the mechanism. They are widely used in surgical manipulators and precision optical-mechanical systems. This paper introduces a new family of planar mechanical linkages that generate a geometrically exact RCM. The adaptability of this linkage family is leveraged to extend the performance limits of flexure-based RCM pivots by compensating for parasitic motion, improving restoring torque linearity, and enhancing radial stiffness and angular stroke. Three planar flexure-based kinematic implementations are investigated. The first realizes an exactly constrained flexure-based RCM pivot with no second-order parasitic motion and nearly constant angular stiffness. The second exploits redundant topologies to suppress parasitic motion while increasing radial stiffness without compromising angular stroke or restoring moment linearity, thereby overcoming a longstanding trade-off in overconstrained flexure pivot design. The third enables a large-stroke flexure pivot allowing ±45° rotation without internal degrees of freedom and minimized parasitic motion. By intentionally exploiting parasitic effects, the stiffness of this large-stroke pivot can be continuously tuned. For each configuration, a direct analytical model is developed to predict its key kinetostatic properties. The models are validated through numerical simulations and demonstrate how parasitic motion can be treated as a controllable design parameter to extend the performance limits of flexure-based RCM pivots.

Keywords: Remote center of motion, Compliant mechanism, Flexure-based pivot, Parasitic shift

1 Introduction

Remote Center of Motion (RCM) mechanisms are single-degree-of-freedom (1-DoF) pivot systems that constrain the rotation of an output stage about a fixed axis located outside the physical structure of the mechanism [1]. In contrast to conventional revolute joints—where the axis of rotation corresponds to a tangible physical component, such as the shaft of a journal bearing—the rotational axis in RCM mechanisms is purely geometric in nature. For this reason, it is commonly referred to as a virtual axis of rotation. RCM mechanisms are commonly used when a payload such as a probe or an optical component needs to be pivoted about an axis passing through its own physical structure. In a planar reference frame, this virtual axis reduces to a fixed point, referred to as the Center of Rotation (CoR). For an ideal RCM mechanism, the Instantenous center of rotation (ICR) remains fixed for all configurations; the CoR denotes this fixed point, evaluated at the nominal position.

Among single-degree-of-freedom (DoF) RCM architectures, parallelogram linkages are widely employed, as they are the only four-bar mechanisms capable of exactly transmitting rotational motion between two links [2]. Such RCM kinematics are frequently used in minimally invasive surgery systems [3] and provide a solution to align the rotation axis of exoskeleton links to the human joints axis [4]. While RCM mechanisms based on parallelogram architectures exist in many forms, this paper introduces a new family of parallelogram-based RCM configurations that expands their design space.

Flexure pivots are an alternative approach to plain or rolling rotational bearings. Their working principle relies on elastic deformation of slender elements instead of friction or rolling contacts between solids. Compared with traditional bearings, flexure mechanisms eliminate friction, backlash, wear and the need for lubrication or assembly. Advantageously, flexure-based mechanisms can replicate complex planar kinematics while remaining monolithic, scalable, and readily manufacturable, making them well suited for miniaturization. These attributes enable high precision, long operational life, and suitability for demanding environments such as vacuum, liquid immersion, or extreme temperature. Consequently, flexure pivots have found wide use in precision positioning systems [5], medical devices [6], aerospace environment optomechanical pointing mechanisms [7–9], robotic wrists and robotic assembly manipulators [10–12], small-scale MEMS devices [13], high-sensitivity load cell designs [14], and horological oscillators [15–17]. Despite these advantages, the application of flexure pivots remains limited by four key challenges: limited angular stroke, parasitic shift, non-linear elastic restoring moment, and reduced radial stiffness away from neutral position.

Research on flexure pivots dates back to the 1950s [18], leading to a wide range of configurations [19–21]. However, replacing physical revolute joints with flexures introduces a deterministic parasitic translation of the center of rotation (CoR), which compromises absolute positioning accuracy. In planar cross-spring pivots, the leading-order parasitic shift scales with the square of the rotation angle and occurs along the symmetry axis of the pivot [22]. Consequently, all fully planar cross-spring pivot, referred to as Remote Center of Compliance (RCC) pivots, exhibit second-order parasitic shift, preventing strictly kinematic RCM behavior and restricting their use primarily to micropositioning applications. Similar limitations arise in flexure-based realizations of classical RCM kinematics implemented using simple notch hinges [23,24]. In practical systems, such geometric effects can introduce significant measurement noise, for example through tilt-to-length coupling in precision laser interferometers where optical mirrors are often mounted on flexure pivots [25,26].

Two main strategies have been proposed to mitigate parasitic

[1]Corresponding Author.
Version 1.18, June 1, 2026

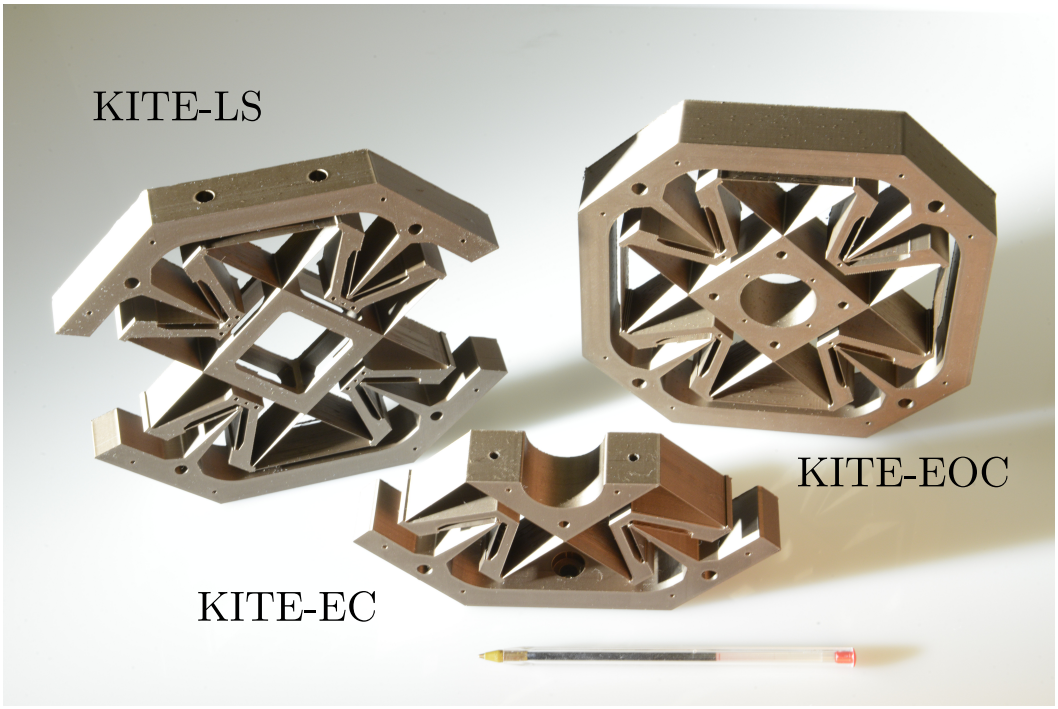

Fig. 1 Photograph of three monolithic flexure pivots from the KITE family, fabricated by 3D printing. KITE-LS (±45° large-stroke pivot with minimized parasitic shift), KITE-EC (±22.5° exactly constrained RCM pivot with no second-order parasitic shift), and KITE-EOC (±22.5° exactly-overconstrained pivot with enhanced radial and out-of-plane stiffness and near-zero parasitic shift).

shift in flexure pivots: kinematic overconstraint and geometric compensation. The first relies on adding radial or auxiliary flexure elements to suppress undesired motion [27,28]. While effective in eliminating parasitic CoR shift, these planar designs are overconstrained in the sense that their DoF exceeds their mobility predicted by the standard planar mobility formula. Overconstraint generally results in elevated internal stresses, highly nonlinear moment-rotation characteristics, reduced admissible angular stroke, and increased sensitivity to manufacturing tolerances, which together complicate actuation and limit performance [29]. Nevertheless, overconstrained flexure pivots offer several key benefits, such as higher radial and axial stiffness, improved resistance to buckling, and, in principle, completely eliminating parasitic motion when subjected to pure moment loading. As a result, many planar flexure pivots reported in the literature that exhibit near-zero parasitic CoR shift rely on overconstrained architectures [5,30,31].

The second strategy suppresses parasitic translation through geometric compensation. For applications where restoring moment linearity is critical, such as improved isochronism in horological oscillators [17] or fast steering mirror actuation [32], specific exactly constrained topologies have been proposed. A well-known result due to Wittrick [18] shows that arranging two crossed flexure beams in parallel planes with a crossing ratio of $1/2-\sqrt{5}/6 \approx 0.127$, called Wittrick's crossing ratio (Fig. 6a), cancels second-order parasitic translation of the CoR. When combined with an appropriate choice of crossing angle, these configurations also minimize nonlinearities in the restoring moment, an important criterion in horological oscillators [33], and precision pointing devices [34]. This concept has been extended to exactly constrained RCM pivots that compensate parasitic shift in a similar manner [35]. More generally, numerical optimization of flexure beams in two distinct planes has also been employed to reduce parasitic motion of RCM pivot while maintaining exact constraint [36].

However, in fully planar implementations where all flexures lie in a single plane, geometric compensation strategies typically rely on serial arrangements of flexure elements to achieve parasitic cancellation [5,37–39]. Such serial architectures introduce internal degrees of freedom of the intermediate stages, which degrade dynamic performance. Even under static loading, load-dependent stiffness of the internal DoF's can compromise absolute accuracy, whereas exactly constrained mechanisms are less prone to these effects. To mitigate these limitations, internal degrees of freedom are often constrained using coupling kinematics, for example in serial architectures combining RCC pivots [11,29] or rectilinear stages [40]. More recently, exactly constrained planar flexure pivots achieving zero parasitic shift with increased angular stroke have been reported, though they require flexure elements spanning 360° around the CoR and optimization to maintain constant stiffness characteristics [16,19,41]. Nevertheless, no fully planar flexure pivot has yet combined exact RCM kinematics, geometric parasitic shift compensation, high radial stiffness, and extended angular stroke within a single reconfigurable architecture.

This article presents the KITE pivot family (patent pending), a new class of fully planar RCM flexure pivots generating a center of rotation located outside the physical structure with no parasitic shift. The underlying rigid-body mechanism is a new family of parallelogram-based linkages satisfying exact RCM conditions, which provides the kinematic foundation for the compliant implementation. The flexure realization is further optimized to suppress second-order parasitic CoR shift while preserving compactness and high radial stiffness. The reconfigurability of the proposed architecture gives rise to three configurations, shown in Fig. 1, each designed to push a distinct performance limit: maximizing angular stroke (KITE-LS), minimizing parasitic translation of the rotation axis (KITE-EC), and maximizing radial and out-of-plane stiffness (KITE-EOC). The main contributions of this article are organized as follows.

Section 2 introduces a new class of planar RCM mechanisms derived from parallelogram linkages. The generic rigid-body topology is formulated, and the conditions required to achieve geometrically exact circular motion are established. Representative configurations are then presented and reconfigurability is discussed.

Section 3 presents the flexure-based embodiment of the generic RCM mechanism. Rather than directly replicating rigid joints, the compliant architecture is designed to preserve the underlying 1:1 transmission condition responsible for exact RCM behavior. The key geometric features are identified, and an analytical nonlinear model is developed to predict the principal kinetostatic properties of the flexure pivot, including parasitic translation shift, rotational stiffness, and admissible angular stroke. Maintaining the analogy with rigid-body linkages, a new class of flexure architectures termed *exactly-overconstrained* is introduced, which overcomes longstanding trade-offs between support stiffness, moment linearity, and angular stroke in overconstrained flexure design.

Section 4 validates and discusses three representative flexure topologies through finite element simulations. The first topology realizes a fully planar, exactly-constrained RCM pivot exhibiting zero second-order parasitic motion and nearly constant rotational stiffness. The second topology leverages redundant kinematics to create an exactly-overconstrained architecture. This enables simultaneous suppression of CoR shift and significant increases in radial and axial stiffness without degrading restoring moment linearity or angular stroke. The third topology achieves a large-stroke pivot with a rotational range of ±45°, while preserving minimizing parasitic motion; its stiffness can additionally be tuned through a preload mechanism.

2 New Family of RCM Rigid-Body Kinematics

This section introduces the generic rigid-body kinematics of the planar RCM mechanism, which can be readily used in classical mechanics and serves as the foundation for the later flexure-based design. In this article, architecture are classified using their mobility in the classical sense of Chebychev-Grübler-Kutzbach planar mobility criterion:

$$M = \sum_{i=1}^{n} d_i - 3b \tag{1}$$

where d_i is the sum of the degrees of freedom of all the articulations in the mechanism (i.e the number of pivots in the following kinematics) and b the number of kinematic loops equal to $b = d_i - n + 1$ where n is the number of rigid links in the mechanism [29].

For the planar 1-DOF RCM kinematics presented below, the mechanism is considered exactly constrained if $M = 1$, underconstrained if M>1, and over-constrained if M>1.

2.1 Generic Exactly-constrained Configurations. Figure 2 illustrates the generic planar rigid-body kinematics of the *KITE* RCM pivot family. Two exactly-constrained configurations are presented:

- Four coupler link configuration (Section 2.1.2, Fig 2a): Based on four parallelograms sharing a common vertex.
- Three coupler link and one homokinetic coupling configuration (Section 2.1.2, Fig 2b): Based on three parallelograms sharing a common vertex and a homokinetic coupling between the two base revolute joints, thereby forming a fourth parallelogram.

Both configurations require ten revolute joints and eight links, forming three kinematic loops and providing a mobility of one and a single DoF. These linkages are both perfect remote center of motion (RCM) mechanism in which the mobile stage is constrained to rotate about a fixed virtual center of rotation O relative to the base. The perfect rotational motion relies on the perfect 1:1 transmission ratio provided by the four parallelogram four-bar linkages. This type of RCM differs from all known planar mechanisms [2] in that the moving part is supported by three (Fig 2b) or four links (Fig 2a), whereas existing mechanisms have two. To guarantee exact rotational motion of the mobile stage, the four conditions of Section 2.1.1 or the fives of Section 2.1.2 must be satisfied, depending on the chosen configuration.

2.1.1 Four coupler link configuration .

(1) **Base revolute joints:** Two rigid links (called base links 12 and 34) are connected to the base by two revolute joints, respectively D_{12} and D_{34}, placed arbitrarily in the plane.
(2) **Remote center of rotation:** The remote center of rotation O is selected at an arbitrary location in the plane, not coinciding with D_{12} or D_{34}.
(3) **Mobile stage:** A rigid stage is introduced, incorporating four revolute joints B_1, B_2, B_3, and B_4, none of which coincide with D_{12} or D_{34}. Each pair of revolute joints, respectively (B_1, B_2) and (B_3, B_4), connects the moving stage to the same base link, respectively 12 and 34, and must be located at distinct positions $(B_1 \neq B_2)$ and $(B_3 \neq B_4)$.
(4) **Coupler links:** Four rigid links (called coupler links 1, 2, 3, and 4) are attached at one end to B_1, B_2, B_3, and B_4, respectively, and at the other end to output links 12, 12, 34, and 34 via four revolute joints C_1, C_2, C_3, and C_4, respectively. These joints are arranged such that the four quadrilaterals $OB_iC_iD_i$ form parallelograms.
Note: This geometric constraint imposes a unique possible position for C_1, C_2, C_3, and C_4.

2.1.2 Three coupler links and one homokinetic base coupling configuration .

(1) **Base revolute joints:** Two rigid links (called base links 12 and 3) are connected to the base by two revolute joints, respectively D_{12} and D_3, placed arbitrarily in the plane.
(2) **Remote center of rotation:** The remote center of rotation O is selected at an arbitrary location in the plane, not coinciding with D_{12} or D_3.
(3) **Mobile stage:** A rigid stage is introduced, incorporating three revolute joints B_1, B_2, and B_3, none of which coincide with D_{12} or D_3. The pair of revolute joints (B_1, B_2) that connects the moving stage to the same base link 12 must be located at distinct positions $(B_1 \neq B_2)$.
(4) **Coupler links:** Three rigid links (called coupler links 1, 2, and 3) are attached at one end to B_1, B_2, and B_3, respectively, and at the other end to output links 12, 12, and 3 via three revolute joints C_1, C_2 and C_3, respectively. These joints are arranged such that the three quadrilaterals $OB_iC_iD_i$ form parallelograms.
(5) **Homokinetic coupling:** An additional link (called base joints coupler link 1) is connected to the base links 12 and 3 via two revolute joints E_1 and F_1, respectively, such that the quadrilateral $D_{12}D_3F_1E_1$ forms a parallelogram.
Note: This geometric constraint ensures that the rotations of D_{12} and D_3 always remain equal.

Two rigid-body implementations of the mechanisms with coincident revolute joints are shown in Fig. 2b–c.

Interestingly, out-of-phase parallelogram configurations, defined by differing initial OBD angles among two of the four $OB_iC_iD_i$ parallelograms, eliminate singular configurations that may cause mechanism locking and restrict the workspace. Remote linear or rotational actuation can be directly coupled to a single base joint D whose rotation is perfectly synchronized with that of the stage around O (Fig. 16c).

2.2 Over-constrained configurations. Because rigid-body kinematic rely on parallelogram linkages, many over-constrained configurations are possible. Redundancies can be introduced by adding parallelogram-type couplings, either at the virtual center of rotation, where two parallelograms $OB_iC_iD_i$ and $OB_jC_jD_j$ connected to an additional base revolute joint D_{ij} are added (Fig. 3a), or between two base revolute joints by adding a coupler link E_iF_i

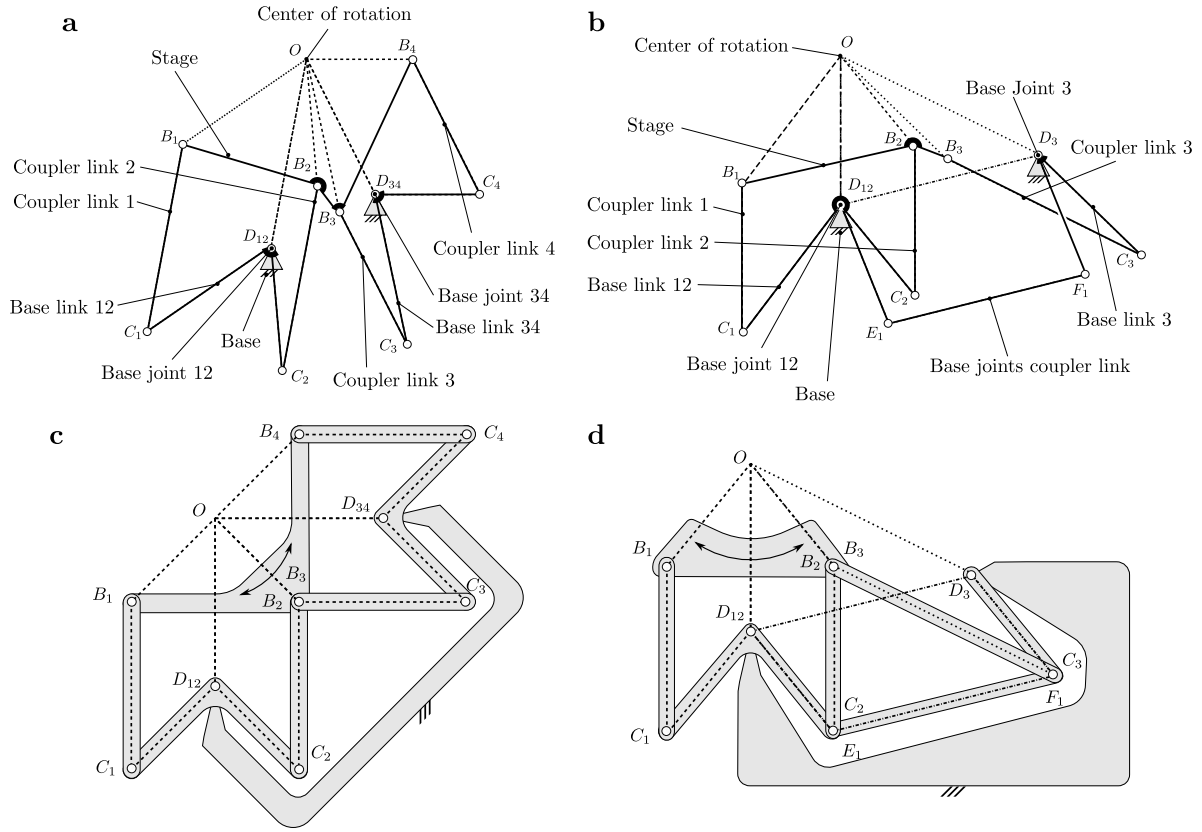

Fig. 2 Generic designs of geometrically exact RCM linkage with a mobility of M=1. (a) Four coupler links configuration. (b) Three coupler links and one homokinetic coupling configuration. (c) and (d) show rigid-body implementations options with coincident joints.

(Fig. 3 b). These additional links increase the load-bearing capacity of the mechanism, particularly for the flexure-based kinematics. In planar linkages with identical parallelograms(Fig. 2 **c**), an additional coupler link E_iF_i prevents singularities via out-of-phase coupling between the base joints (Fig. 3**b**). However, these redundant links increase tolerance sensitivity, complicate assembly, and may cause binding or locking, reducing reliability.

2.3 Large-stroke configuration. Configurations that maximize rotation of the mobile stage relative to the base revolute joints increase the range of motion when the mechanism uses flexure joints. A widely adopted approach to increase the achievable stroke is to employ a serial configuration, as illustrated in Fig. 4**a**, obtained by combining two single-degree-of-freedom RCM mechanisms that share a common center-of-rotation (CoR) point. This results in a two-degree-of-freedom kinematic system (one for the rotating stage and one for the intermediate stage). But Adding a coupling link between two base links, as shown in Fig. 4**b**, constrains the mechanism to a single degree of freedom and eliminates the undesired internal Dof. The 1:–1 inversion function of the coupling link (which couples rotation with a Watt's linkage) effectively doubles the rotation of the mobile stage relative to the intermediate stage.

It should be noted that if the configuration (**a**) is realized in two orthogonal planes rather than in a single plane, this rigid-body kinematics yields a 2-degree-of-freedom RCM universal joint, or tip-tilt stage, with no internal degrees of freedom and featuring two orthogonal axes of rotation.

3 KITE Flexure-based Kinematic

As described before, RCM mechanism kinematics is built with four coupler links and two base revolute joints. The implementation of the rigid-body linkages into a flexure mechanism is carried out as follows:

- **Base flexure joints**: Each base revolute joint in the rigid-body mechanism is substituted with a flexure-based cross-spring pivot whose instantaneous center of rotation coincides with the point D_{ij} specified in the linkage design. The geometry of these cross-spring pivots is characterized by the following dimensions, as illustrated in Fig. 5 **a**: the length of both beams L_p, their out-of plane width b, their thickness t, the normalized distance η between the center of rotation and the beam ends attached to the rotating stage, and the semi-angle between the beams α. Examples of cross spring pivots and their corresponding instantaneous centers of rotation are provided in Fig. 5**a**. Note that when $\eta \leq 1$ the flexure pivot design requires two distinct planes.

- **Coupler links**: Each coupler link is replaced by a single beam element of length L, as shown in Fig. 5**b**. with out-of-plane width b, and thickness t .

To ensure that the RCM flexure pivot exhibits a single degree of freedom (DoF), the geometric ratios $b/t > 10$ and $L/t > 10$ must, at a minimum, be satisfied [29]. If these conditions are met, the mobility of the flexure-based mechanism can be considered identical to its rigid-body linkage counterpart given by Eq.1.

The full flexure implementation of an exactly-constrained RCM pivot, named KITE-EC, is shown in Fig. 6 with the pivot points corresponding to the rigid-body linkage from Fig. 2**a**. Note that in the flexure-based design, B_2 and B_3 are not coincident, but this is not a necessary condition as shown in Fig. 2**a**.

Using the same implementation rules, a ten times over-constrained design, the large-stroke configuration of Fig. 4**b** and a

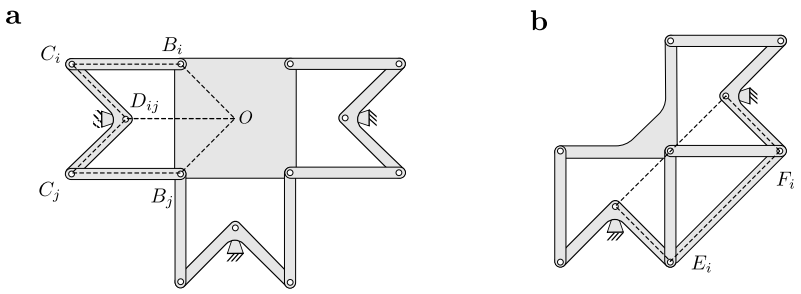

Fig. 3 Design of two over-constrained mechanisms with a mobility of M=0

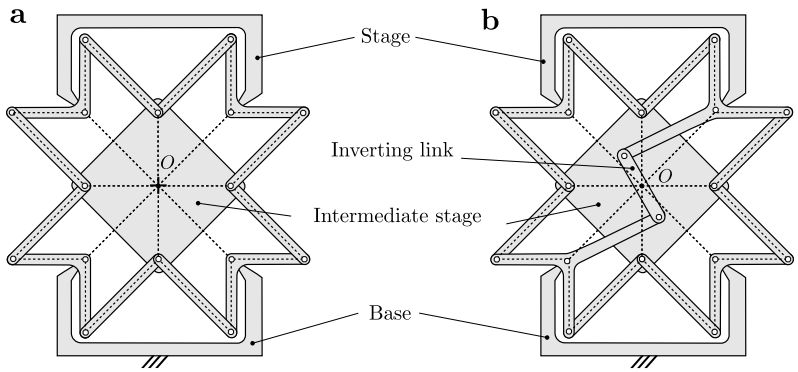

Fig. 4 Design of large strokes pivot mechanisms with a mobility of (a) M = 2 (underconstrained) , and (b) M = 1 (exactly-constrained)

monolithic flexure tip-tilt stage with minimized parasitic shift are implemented as illustrative examples in Appendix A.

3.1 Kinetostatic Analytical Model. Unlike four-bar linkages, flexure-based mechanisms exhibit parasitic motion, inherent stiffness, and a limited range of motion. This section introduces analytical models for parasitic motion, rotational stiffness, and maximum beam stresses in the KITE flexure pivot. These values enable rapid preliminary dimensioning.

Since parasitic shift depends directly on the quality of the 1:1 motion transmission between the center of rotation and the base revolute joints (maintained by parallelograms in the rigid-body linkage) a dedicated flexure kinematic model is developed for the 1:1 transmission building block. The analytical models for the cross-spring pivots used in the RCM design are available in [22,29] and reproduced in Appendix B for reference.

The four assumptions underlying the analytical models are:

(1) Euler–Bernoulli beam theory applies, implying small deflections, negligible shear deformation, and a continuous, isotropic, linear-elastic material.
(2) In the geometric kinematic model, beam forces (tension and compression) in all beams are negligible, based on the assumption that the beams are slender and exhibit much greater stiffness in axial loading than in bending.
(3) The center of rotation of a cross-spring flexure pivot translates proportionally to the square of the rotation angle, θ, in the direction of its symmetry axis, with higher-order terms neglected.
(4) More generally, the nonlinear kinematic analysis of the flexure-based RCM pivot is developed up to the second order of motion, with higher-order terms neglected.

3.1.1 Parasitic Translation Shift Optimization. While 1:1 transmission is straightforward in rigid-body parallelogram linkages, it becomes more challenging when the coupler links and base joints are implemented as flexures, due to parasitic motions that introduce nonlinear geometric relationships. These nonlinearities arise from two sources: the trigonometric dependence of rigid-link positions and the apparent axial shortening of the flexures under bending. This shortening results from both axial strain and the geometric effect of neutral-axis curvature. In this study, axial strain is neglected due to the low bending-to-axial stiffness ratio of the beams; only the second-order geometric shortening induced by bending is retained. Figure 7 **a** shows the flexure parallelogram building block of the KITE pivot, labeled $OBCD$. To minimize parasitic translation of the KITE, the transmission ratio between the instantenous center of rotation D under an applied angle θ_D to the point O should be of 1:1. As detailed in [42], this transmission constancy depends on the parasitic motion of the base revolute joint λ_p and the axial shortening of the coupling beam λb. The rigid lever length H and the offsets between rotation point and the clamped ends of the beam R should be equal in both levers to preserve the desired parallelogram topology.

The transmission error of the flexure-based parallelogram is defined as the difference between the rotation of the center of rotation O and the applied rotation at D :

$$\Delta\theta = \theta_\mathrm{O} - \theta_\mathrm{D} \tag{2}$$

Using kinematic loop-closure equations along the x axis, expanded to second-order for the deformed flexure parallelogram, the following relationships is obtained:

$$\Delta\theta = \frac{\lambda_\mathrm{b} - \lambda_\mathrm{p}}{H} \tag{3}$$

The parasitic translation of the flexure pivot center of rotation, λ_p, has been well studied [18,22]. These studies show that the the leading order of parasitic translation along the pivot symmetry axis is proportional to the square of the rotation angle:

$$\lambda_\mathrm{p} = k_\mathrm{p} L_\mathrm{p} \theta^2, \tag{4}$$

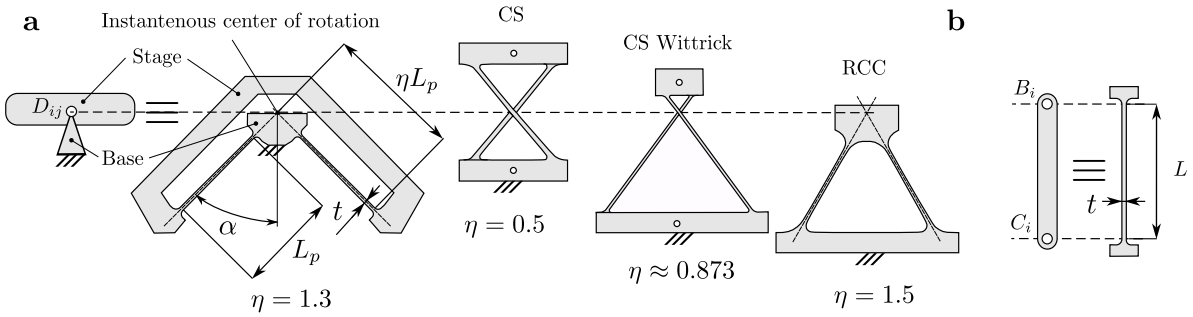

Fig. 5 (a) Flexure implementation options for the base revolute joints D_{ij}: a cross-spring pivot (CS) spanning two separate planes ($\eta < 1$); a cross-spring pivot at Wittrick's ratio (CS Wittrick, $\eta \approx 0.873$); and a single-plane cross-spring pivot with remote center of compliance (RCC, $\eta > 1$). (b) Flexure implementation of the coupler link $B_i C_i$.

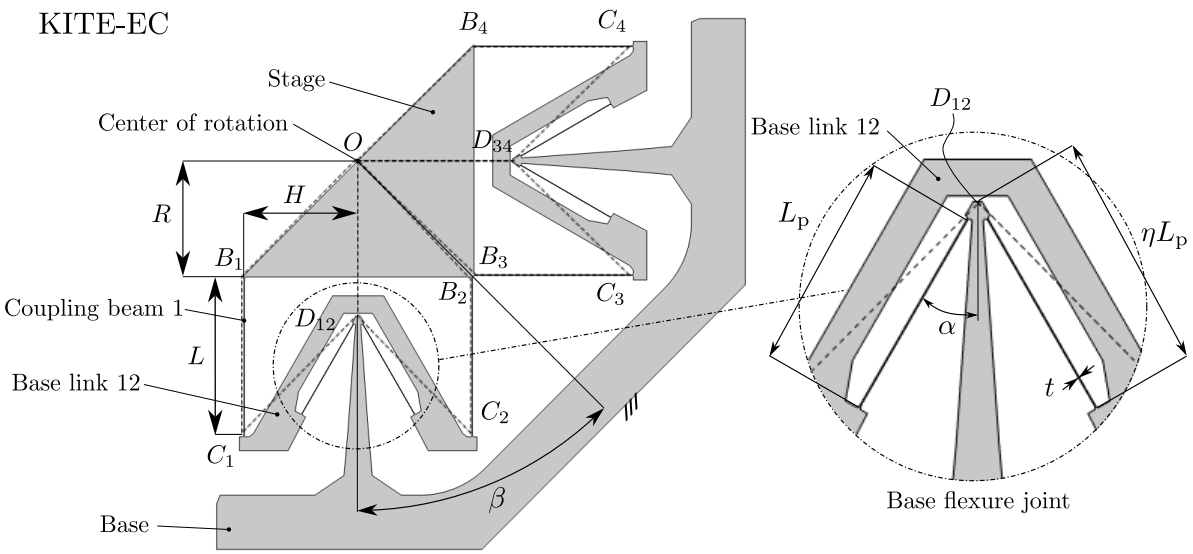

Fig. 6 Flexure implementation and dimensions of the KITE-EC, an exactly-constraint flexure-based RCM pivot.

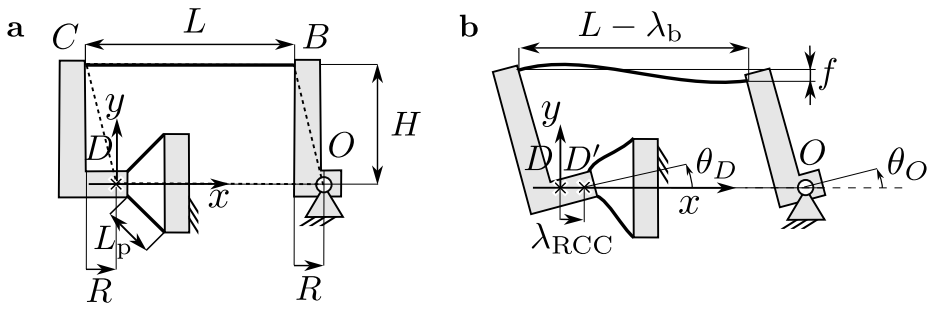

Fig. 7 Flexure implementation of one ($OBCD$) parallelogram linkage used to build the KITE pivots. The 1:1 transmission between θ_O and θ_D is optimized to eliminate second-order parasitic shift of the flexure pivot (a) in neutral position, (b) deformed with an angle θ.

where k_p is a constant determined by the flexure pivot dimensions. For a generic cross-spring pivot, the value of k_p is provided in Appendix B.

The second-order axial shortening of the coupling beam, λ_b, is detailed in [42] and provided for this specific case in Appendix C. The resulting expression gives:

$$\lambda_b = \frac{1}{10} L\theta^2. \tag{5}$$

Finally, for the KITE-EC pivot composed of four identical parallelograms with a semi-angle β shown in Fig.6, the second-order parasitic shift, in the β direction, can be expressed in function of $\Delta\theta$ using:

$$\lambda = \frac{H\Delta\theta}{\cos(\beta)} = \frac{\left(\frac{1}{10}L - k_p L_p\right)}{\cos(\beta)}\theta^2 + O(\theta^3) \tag{6}$$

This leads to the following condition for the coupling beam length that eliminates second-order parasitic motion :

$$L_{opti} = 10\, k_p L_p. \tag{7}$$

Remark: If an additional coupling beam E_1F_1 is introduced between two base flexure joints (Fig. 10), this compensation is automatically satisfied by symmetry. Indeed, the projections of the parasitic translations from both base flexure pivots compensate the axial shortening of the additional coupling beam E_1F_1. More generally, in asymmetrical topologies, each parallelogram in the rigid-body kinematics should be dimensioned to optimize 1:1 transmission constancy in order to eliminate second order parasitic shift based on [42].

3.1.2 Rotational Stiffness. The rotational stiffness of the RCM mechanism defines its restoring behavior and dynamic response. In flexure-based mechanisms, it arises from the combined elasticity of the flexure pivots and coupling beams. This section also shows how second-order parasitic motions can be exploited to continuously tune the flexure pivot stiffness using an external constant force.

The rotational stiffness the coupling beam calculated from its strain energy is:

$$K_{\theta,b} = \frac{12EI}{L} \tag{8}$$

where E is the Young's modulus and I is the second moment of area of the beam cross-section. The total angular stiffness of the RCM pivot is the sum of contributions from the coupling beam C_iB_i and the base flexure RCC pivots D_i:

$$K_\theta = n_b K_{\theta,b} + n_p K_{\theta,p} \tag{9}$$

where $K_{\theta,p}$ is the stiffness of one base RCC pivot (Appendix B) and n_b and n_p denote the number of coupling beam and the number of base flexure joints, respectively.

Stiffness tuning enables performance optimization across dynamic and quasi-static applications. In dynamic systems, it allows control of the natural frequency—matched to a target oscillation in horological mechanisms, or detuned to avoid resonance with base excitations in aerospace and precision systems. In quasi-static applications, near-zero stiffness flexure pivots can be exploited for extremely high sensitivity in sensors or load cells [14], while also providing passive vibration isolation through inherent mechanical filtering [21]. The stiffness of the large-stroke KITE-LS flexure pivot can be tuned by applying a constant force to the base links. This is achieved by a preload mechanisms that exert a constant force directed toward an opposing base link throughout the motion (Fig. 13). The potential energy associated with this preload decreases as the stage moves, so the total potential energy of the mechanism can be expressed as the sum of elastic energy in the beams and the negative preload contribution:

$$U_{tot} = \frac{1}{2}K_\theta\theta^2 - n_{preload}N\lambda_t \tag{10}$$

where $n_{preload}$ denotes the number of preload base links and λ_t represents the second-order relative motion of the base links. The latter corresponds to the parasitic motion of a two-parallel-leaf-spring stage, the value of which can be found in [29]:

$$\lambda_t = \frac{3}{5}L\theta^2 \tag{11}$$

By differentiating the total potential energy twice with respect to rotation, the effective angular stiffness of the preloaded KITE-LS pivot is derived:

$$K_{\theta,preload} = K_\theta(1 - \frac{N}{N_0}) \tag{12}$$

where N_0 denotes the preloading constant force that renders the stiffness of the RCM pivot equal to zero:

$$N_0 = \frac{5}{6}\frac{K_\theta}{n_{preload}L} \tag{13}$$

3.1.3 Admissible Angular Stroke. The admissible stroke is constrained by the maximum admissible stress σ_{adm} in the material, which is typically required to remain below the fatigue limit to ensure an infinite number of loading cycles. The admissible stroke of cross-spring flexure pivot is given in Appendix B.

The maximum stress of the coupling beam is calculated using the approximated deformed state of the beam. This gives its admissible angle as:

$$\theta_{\text{adm}} = \pm \frac{\sigma_{\text{adm}} L}{3Et} \tag{14}$$

To design the RCM flexure pivot, both admissible strokes (base RCC and coupling beam) must be at least equal to the desired stroke of the pivot.

The envelope size of the pivot, determined primarily by the length of the coupling beams L, scales with the desired stroke θ_{adm} and beam thickness t, and is inversely proportional to the material parameter σ_{adm}/E. This ratio typically ranges from about 0.1% (e.g. aluminum) to 0.7% (e.g. spring steel sheet) for metals and 0.1–2 % for composites and thermoplastics. Consequently, the pivot envelope size is influenced by several factors: the manufacturing process, which sets the minimum achievable beam thickness; the desired maximum rotation angle; and the material properties.

3.1.4 Radial Stiffness. The radial stiffness of the pivot K_r is evaluated along the symmetry axis of the pivot in the plane of the flexure, assuming the rigid bodies (stage, base link, and base) are infinitely stiff. An analytical model can be derived by treating the KITE-EC as a spring network: the base flexure joint and coupling beams act in series, and the two symmetric halves of the mechanism are in parallel. This yields the following expression for the radial stiffness:

$$K_r = \frac{4\cos(\beta)^2 tbE}{L + \frac{L_p}{\cos(\alpha)^2}} \tag{15}$$

For the KITE-EC pivot shown in Fig. 6, the corresponding buckling-critical compressive load on the stage is equal to twice the Euler critical load of an idealized, fixed–fixed beam:

$$N_c = \frac{8\pi^2 EI}{L^2} \tag{16}$$

3.2 Exaclty-overconstrained Flexure-based Mechanisms. This section presents a new classification of compliant mechanisms, called "exactly-overconstrained", which allows the concept of overconstrained mechanism in traditional kinematics to be extended to the case of compliant systems.

We define an exactly-overconstrained flexure mechanism as a compliant mechanism that:

(1) intentionally incorporates redundant kinematic chains ($M <$ DOF), while preserving the desired degree(s) of freedom and exhibiting no undesired internal degrees of freedom;
(2) is derived from an exactly-constrained mechanism exhibiting at least zero second-order parasitic motion of the output stage.

If these two conditions are satisfied, an exactly-overconstrained flexure mechanism can be interpreted as the compliant counterpart of a traditional overconstrained kinematic system, such as a multi-hinged door ($M < 1$). In such rigid-body mechanisms, the repetition of constraints enables load sharing between joints, thereby increasing load-bearing capacity, while joint clearances accommodate geometric incompatibilities due to misalignment. In compliant mechanisms, where no such play exist, compatibility must instead be ensured by design; in particular, the elimination of competing parasitic motions is required to avoid the buildup of internal stresses and preserve the intended kinematic behavior.

This definition distinguishes exactly-overconstrained mechanisms from classical overconstrained compliant architectures, in which redundant constraints typically introduce internal stress, nonlinear stiffening, and reduced stroke due to geometric incompatibilities arising from competing motions of the flexure elements.

In this work, the definition is restricted to single-DOF planar mechanisms, and more specifically to flexure pivots. It should also be noted that manufacturing tolerances and temperature gradients are not considered here, although they may introduce internal stresses in practice.

Finally, several existing compliant mechanisms can be interpreted within this framework. These include overconstrained cross-spring pivots with more than two leaf springs with a Wittrick's crossing ratios of 0.127 (or 0.873) [30], as well as the overconstrained rectilinear stage proposed in [43]. The RCM topologies presented in [35] could similarly be extended through radial replication to realize exactly-overconstrained pivot architectures.

4 FEM Validation and Discussion

This section validates the analytical models (AM) developed in Section 3.1 against finite element simulations (FEM) for three KITE pivot configurations, each targeting a distinct performance objective: exactly-constrained RCM with zero second-order parasitic shift (KITE-EC), high support stiffness with zero parasitic shift (KITE-EOC), and large angular stroke with tunable stiffness (KITE-LS). Each configuration is assessed in terms of admissible stroke, parasitic shift, elastic restoring moment linearity, and support stiffness (rotational, radial, and axial).

All FEM simulations were performed in COMSOL Multiphysics 6.2. For in-plane kinetostatic properties, beams were modeled as 2D planar sections (length L, thickness t, width b) using second-order serendipity elements (four through the thickness, 300 along the length) with a plane stress assumption. For the out-of-plane axial stiffness simulations, a 3D mesh sweep of ten elements through the width is used. A linear-elastic material is used. Geometric nonlinearity was included in a stationary study to impose an angle θ to the stage when the base edges have fixed boundary conditions. In the FEM simulations the maximum Von Mises stress, the secant rotational stiffness and the norm of the displacement of the center of rotation OO' values when the admissible angle θ_{adm} is imposed to the stage are used to validate the admissible stroke, rotational stiffness and second-order parasitic shift predictions of the analytical model. In all parasitic shift simulations, only the beam elements are modeled as compliant, with all rigid-body connections assumed perfectly rigid. For axial (out-of-plane) stiffness, the full monolithic geometry is modeled as an elastic solid. For radial and rotational stiffness, both assumptions are evaluated (perfectly rigid connections and full elastic solid) to quantify the contribution of base link compliance.

4.1 Design constraints for comparison with cross-spring pivots. To put the mechanical performance of the KITE pivot family into perspective, it is compared against well-known cross-spring pivot architectures (Appendix B) under identical design constraints:

(1) Material: All designs and simulations use Böhler steel[2] with Young's modulus $E = 196$ GPa, Poisson's ratio $\nu = 0.3$, and an endurance limit of $\sigma_{\text{adm}} = 800$ MPa.
(2) Beam cross-section: All beam thicknesses are set to $t = 0.1$ mm and widths to $b = 10$ mm, consistent with wire EDM manufacturing.
(3) Stage dimensions: The dimensions of the rotating stage is the same in the flexure-based mechanisms (KITE-EC, KITE-EOC, RCC, RCC-OC pivots) assuming the required platform area is given as a design specification.
(4) Admissible stroke: All pivots are compared at equivalent admissible angular stroke, which defines the beam lengths. The admissible stroke is set to ±22.5° for the KITE-EC and RCC, and to ±45° for the large-stroke configurations (KITE-LS and CS-Wittrick pivots).

4.2 KITE-EC Exactly-constrained RCM Flexure Pivot. This section validates the KITE-EC kinetostatic properties, introduced in Section 3. To assess its performance, it is compared

[2] DIN 220CrVMo13-4

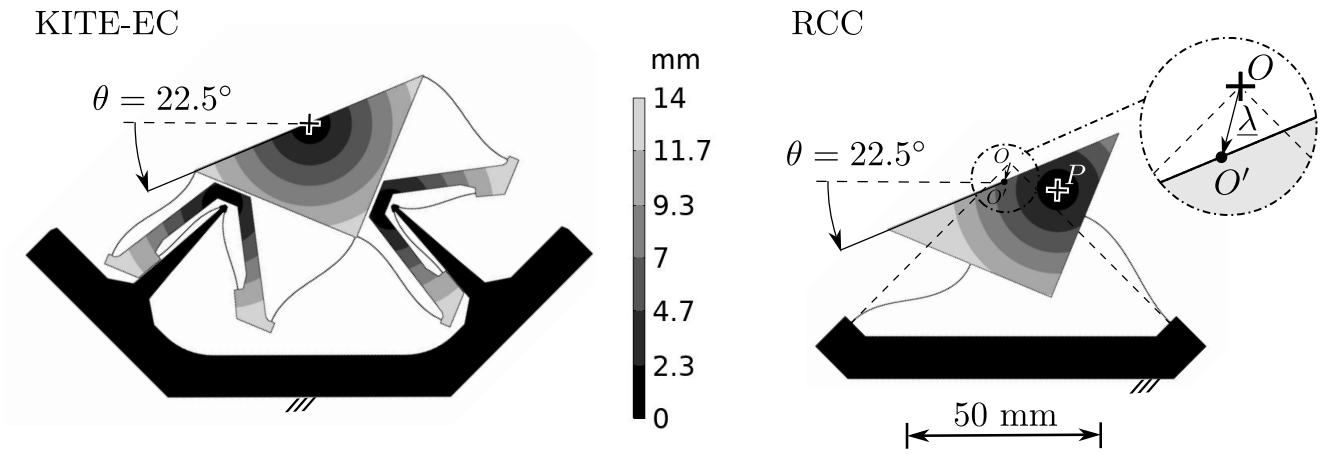

Fig. 8 FEM displacement fields of the optimized RCM and analogous RCC pivot when a 22.5° angle is imposed.

Table 1 KITE-EC Dimensions

L_{opti} [mm]	H [mm]	R [mm]	t [mm]	b [mm]	β [°]	L_p [mm]	η [-]	α [°]	θadm [°]
33.9	25	25.9	0.1	10	45	22.15	1.1	30	22.5

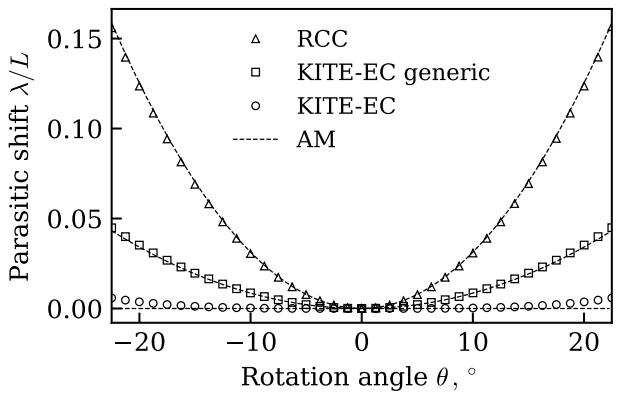

Fig. 9 Normalized parasitic shift of KITE-EC pivots (with and without optimized length of coupling beam *L*) and analogous RCC flexure pivot when an angle *θ* is imposed to the rotation stage.

against a classical RCC pivot designed with the same admissible stroke of ±22.5° and the same rotating stage dimensions. The full dimensions of both pivots are given in Tables 1 and 5, and both configurations are shown in Fig. 8. Table 2 summarizes the FEM results and analytical predictions for maximum stress, secant stiffness, and parasitic CoR shift.

4.2.1 CAD Design considerations. The dimension of the KITE-EC, shown in 6, are chosen by meeting the design constraints of Section 4.1. The beam's length of the base RCC pivot Lp is defined using Eq. B4 and the optimum length of the coupling beam L using Eq. 7. It is then simple to verify that the maximum stress in the coupling beams is lower than the admissible stress of the material using Eq. 14. A rotational repetition of $\beta = 45°$ is adopted to minimize the dependence of radial stiffness on the orientation of a radial force while keeping a planar design. The other geometrical parameters of the base flexure joints are chosen in order to avoid collisions between the rigid bodies trough the motion.

4.2.2 Parasitic shift validation and discussion. To validate Eq. 6, two configurations are compared: a generic KITE-EC (not satisfying Eq. 7) and the optimized KITE-EC. The generic KITE-EC has identical dimensions to the optimized design, except that the parasitic shift direction of the base flexure joints is inverted, so that the contributions of the base joints and coupling beams add constructively rather than canceling. Both configurations are shown in Fig. 9, together with the analogous RCC pivot for reference.

The generic KITE-EC exhibits a nonzero but reduced second-order parasitic shift, well predicted by the analytical model. The optimized KITE-EC eliminates second-order parasitic CoR shift entirely, making it systematically more accurate than any single plane cross-spring pivot regardless of rotation angle. For reference, the RCC pivot exhibits a parasitic translation of the CoR of 6.10 mm at ±22.5°, within 2% of the analytical prediction of 5.97 mm. Note that the instantaneous center of rotation ICR, which corresponds to the minimum of the displacement field at a given angle, does indeed correspond to the CoR (point O) for the KITE-EC, but clearly shifts for the RCC (point P).

A residual parasitic CoR translation remains in the KITE-EC, attributed to axial forces in the beams and to first- and third-order parasitic shift of the base flexure joints, both neglected in the model. As detailed in Fig. 14, this residual remains below 200 μm at ±22.5°, below 50 μm at ±15°, below 10 μm at ±10°, and below 1 μm at ±5°.

4.2.3 Angular stroke and elastic restoring moment validation and discussion. Maximum stress in the beam elements, as revealed by FEM simulations, is underestimated by the analytical model for large deformations, with peak Von Mises stresses of 846 MPa and 899 MPa recorded in the RCC and RCM pivots respectively, compared to the 800 MPa they were designed for. This underestimation is attributed to the axial forces and shear stresses neglected in the analytical model.

At ±22.5°, the secant rotational stiffness of the RCC predicted by the analytical model deviates significantly from the FEM result. Indeed the RCC pivot undergoes a nonlinear 13.3% stiffness reduction, a well-known drawback of the RCC geometry that complicates high-precision actuation. In contrast, this softening effect is not observed in the KITE-EC architecture, which instead shows only a 1% increase in rotational stiffness over the same angular range.

Table 2 KITE-EC and RCC kinetostatic properties

	KITE-EC		RCC	
Mechanical properties at ± 22.5°	AM	FEM	AM	FEM
Max Von Mises Stress σ_{max} [MPa]	800	899	800	846
Secant Rotational Stiffness K_θ [Nmm/rad]	388	392	145	128
Parasitic shift λ [m]	0	193e-6	5.97e-3	6.10e-3

The high restoring-moment linearity of the KITE-EC can be qualitatively attributed to the suppression of parasitic motion. As the parasitic translation of the stage approaches zero, the work associated with this motion and the reaction forces generated by the flexure elements is minimized, resulting in an almost constant apparent rotational stiffness over the motion range. This behavior is analogous to that of cross-spring pivots, where tuning Wittrick's crossing ratio to eliminate second-order parasitic translation similarly yields nearly constant angular stiffness [15,17,34].

4.2.4 Axial and radial stiffness validation and discussion. As shown in Fig. 12 and Tab. 7, the KITE-EC exhibits an axial (out-of-plane) stiffness twice that of the RCC pivot. This improvement is attributed to the increased redundancy of out-of-plane constraints in the KITE-EC architecture.

Regarding radial stiffness, the analytical model (Eq. 15) predicts comparable values for both pivots, with a slight advantage for the KITE-EC. However, the compliance of the base links (assumed rigid in the analytical model) significantly reduces the effective radial stiffness by a factor of 4.9 in FEM. This discrepancy reveals that, despite the base links being significantly thicker than the flexure blades, their compliance is non-negligible for radial stiffness. Good agreement with the analytical model is recovered only when the base links are modeled as perfectly rigid.

Two solutions are proposed to mitigate this effect. First, out-of-plane reinforcements can be added to the V-shaped base links, whose geometry is not optimal for radial stiffness. Second, an alternative configuration (Fig. 16a) eliminates this compliance entirely, though at the cost of requiring an out-of-plane assembly to connect the fixed base. A planar solution consists of adding a single redundant coupling beam (Fig. 13a), which improves radial stiffness by a factor of 3.6 compared to the configuration without the redundant beam.

4.2.5 Application perspectives. Overall, the KITE-EC pivot topology offers the advantage of generating a pivot point outside of its physical structure with no second-order parasitic motion, while maintaining an almost constant rotational stiffness and being exactly-constrained. The suppression of second-order parasitic motion improves the absolute accuracy of the pivot and makes its rotational stiffness largely insensitive to external loads, such as the weight of an object mounted on the moving stage. Moreover, its exactly constrained flexure-based kinematic provides high motion repeatability, a predictable sensitivity to manufacturing tolerances, good dynamic performance, and straightforward assembly when required. The nearly constant rotational stiffness, combined with the RCM characteristics of the pivot, makes it particularly attractive for optical applications, such as fast steering mirrors [32] and optical tables. In this context, parasitic motion could even be deliberately exploited, rather than suppressed, to passively compensate for tilt-to-length coupling noise that arises in several optical systems [44]. In a horological context, this topology could be miniaturized and used to realize a silicon oscillator that is insensitive to gravity orientation and exhibits near-isochronous behavior [15,17].

4.3 KITE-EOC Exactly-Overconstrained Flexure Pivot. This section validates that exactly-overconstrained KITE pivots can simultaneously eliminate parasitic CoR shift and increase stiffness along the kinematically constrained directions of the pivot, without degrading angular stroke or the linearity of the restoring moment. This resolves the long-standing trade-off that typically limits the performance of overconstrained flexure-based mechanisms. To provide a simple reference for how overconstraints typically affect stroke and stiffness linearity in a representative design, we consider an overconstrained RCC-OC mechanism with the same dimensions as those used in the exactly constrained RCC case, as illustrated in Fig. 10. The kinetostatic properties of both KITE-EOC and RCC-OC pivots are presented in Tab.3. The rotational, axial, and radial stiffness values obtained from analytical models and FEM simulations, both based on small-deformation assumptions, are reported in Tab. 7.

4.3.1 CAD design considerations. The exactly-overconstrained KITE-EOC pivot, with a mobility of $M = -5$ (Fig 10), is derived from its exactly-constrained counterpart by applying an axial symmetry, and by adding four redundant coupling beams connecting the base links to further enhance radial and out-of-plane stiffness. The rotational stiffness of the resulting overconstrained RCM is predicted by summing the contributions of the twelve coupling beams and the four flexure base pivots, using Eqs.8 and B3. The admissible angular stroke of the pivot is constrained by the maximum stress in the base flexure pivots given by equ. B4.

4.3.2 Parasitic shift validation and discussion. The first well known advantage of using overconstrained mechanisms is the theoretical elimination of the CoR parasitic shift thanks to symmetrical design. In both RCC-OC and KITE-EOC symmetrical topologies, the parasitic shift from FEM simulations reduces to a few nanometers. This result is not surprising and some other overconstrained designs can claim a similar accuracy [5,31].

4.3.3 Angular stroke and elastic restoring moment validation and discussion. A first notable difference between the overconstrained RCC-OC and the overconstrained KITE-EOC lies in how stress develops in the beam elements with increasing stage rotation. In the KITE-EOC, stress grows linearly, mirroring the behavior of the exactly-constrained KITE-EC case, and the admissible stroke remains identical. In the RCC-OC, however, the overconstraint induces a highly nonlinear stress growth, generating large traction forces in the radial beams. As a consequence, the angular stroke of the pivot is severely limited, reaching only 2.3° at a maximum stress of 800 MPa, which is 8.9 times lower than in the exactly-constrained topology. These traction loads in the radial beams of the RCC-OC also induce a highly nonlinear rise in the elastic restoring moment, as shown in Fig.11, complicating control. Conversely, despite containing more redundant beams ($M = -5$), the restoring moment of the exactly-overconstrained KITE-EOC remains linear and is accurately predicted by the exactly-constrained analytical model.

The limited stroke and pronounced stiffening of the RCC-OC share a common physical origin. When the stage rotates, the redundant constraints enforce geometric compatibility, generating traction forces in the beams that compensate for their geometric shortening due to curvature. These traction forces scale with the longitudinal stiffness of the beams and arise as a second-order effect of the rotation angle ($\propto \theta^2$), causing them to grow rapidly

Table 3 KITE-EOC and RCC-OC kinetostatic properties

	KITE EOC at ±22.5°		RCC-OC at ±2.3°
Mechanical properties	AM	FEM	FEM
Max Von Mises Stress σ_{max} [MPa]	800	889	807
Secant stiffness K_θ [Nmm/rad]	939	949	30067
Parasitic shift λ [m]	0	44.9e-9	4.8e-9

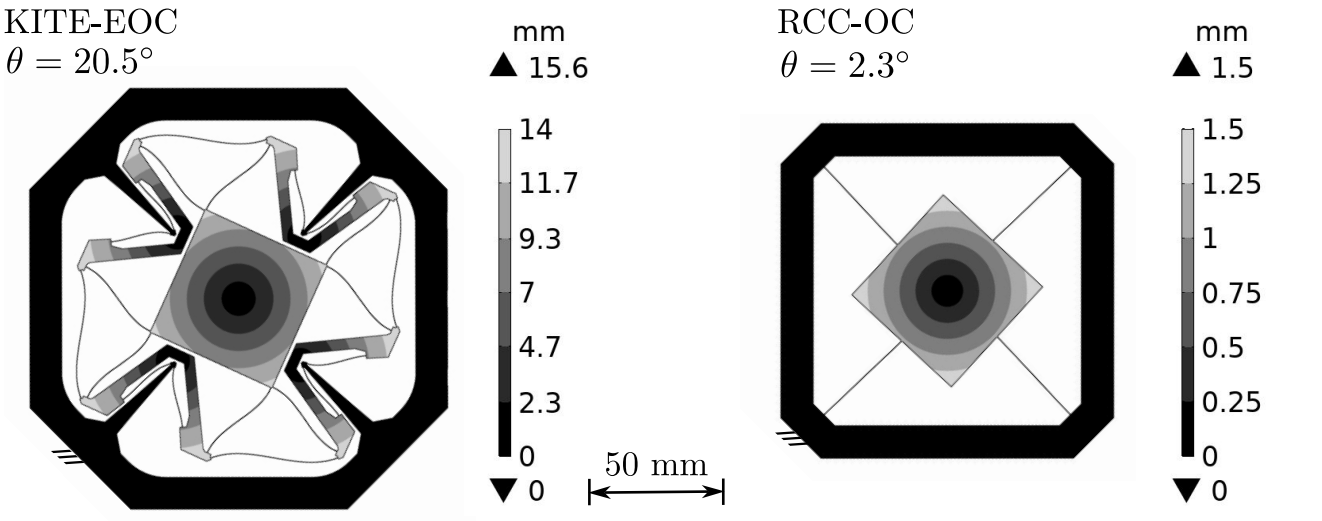

Fig. 10 FEM displacement fields of the KITE_EOC and overconstrained RCC pivot at 2.3° for the same maximum Von Mises stress of 800[MPa].

and nonlinearly with rotation. This produces a steep stress growth that severely restricts the angular stroke, and introduces a dominant third-order contribution to the restoring moment [45], explaining the progressive stiffening observed in Fig. 11.

Suppressing both effects therefore requires eliminating these second-order traction forces, which in turn necessitates removing the underlying second-order parasitic shift. This is consistent with stiffness modeling of cross-spring pivots [28] and parametric studies of overconstrained pivots [30], which show that overconstrained pivots with zero second-order parasitic shift (here classified as exactly-overconstrained) display nearly constant angular stiffness.

In the KITE-EOC, the parallelogram linkages generate no competing second-order motion, so no traction forces arise in the redundant beams and the third-order stiffness nonlinearity is avoided. This suggests that suppressing second-order parasitic motion is a key requirement for introducing kinematic redundancy while delaying the emergence of nonlinear stiffening and stroke reduction in overconstrained compliant mechanisms.

4.3.4 Overconstraint effects discussion. In both the KITE and the RCC, the overconstrained geometries exhibit significantly greater axial stiffness K_z along the rotation axis, by a factor of 27 for the RCC and 21 for the KITE. This considerable effect arises from the fact that the blades opposing the mobile platform are constrained to deform purely in shear along the out-of-plane axis, in contrast to the exactly-constrained case where bending and torsion are constrained by a single blade only. The increase in radial stiffness is less pronounced when comparing the overconstrained and exactly-constrained mechanisms. Adding overconstraints to the KITE increases its radial stiffness by a factor of 3.6, compared to a factor of 1.6 for the RCC-OC. The greater improvement in the KITE geometry is due to the overconstraints limiting the deformation of the base links, as mentioned in Section 4.2.4. When the rigid parts are assumed to be perfectly rigid, the KITE-EOC exhibits a radial stiffness 2.1 times greater than its exactly-constrained counterpart, an expected result given the parallel combination of two KITE-EC mechanisms.

4.3.5 Application perspectives. Overall, these results demonstrate the high effectiveness of overconstraints in simultaneously improving load-bearing capacity and eliminating parasitic shift, with the KITE-EOC emerging as the most performant architecture. While both RCC and KITE geometries benefit significantly from redundancies in axial (×21 for the KITE, ×27 for the RCC) and radial directions (×3.7 vs ×1.6), the exactly-overconstrained KITE-EOC overcomes the stroke reduction and progressive stiffening that have historically limited the practical use of overconstraints in compliant mechanisms. By simultaneously exhibiting high kinematic accuracy, large stroke, low and constant rotational stiffness, and high support stiffness, this architecture addresses a design trade-off in compliant mechanism design, opening new possibilities for applications demanding both precision and load-bearing capacity, such as precision robotics, high-accuracy rotary tables, and space mechanisms. However, predicting the sensitivity of overconstrained designs to geometric deviations remains an open challenge, as no general analytical framework currently exists for capturing their effect in overconstrained compliant mechanisms.

4.4 KITE-LS Large-Stroke Flexure Pivot. This section validates the KITE-LS, a large-stroke flexure pivot achieving ±45° rotation with near-zero parasitic motion and high load-bearing capacity. It is compared against a cross-spring pivot at Wittrick's ratio, which also exhibits zero second-order parasitic shift, designed for the same ±45° admissible stroke. Additionally, the KITE-LS offers rotational stiffness tuning through a simple preload mechanism. The kinetostatic properties of both pivots are summarized in Table 4.

4.4.1 CAD design considerations. The geometry of the KITE-LS pivot, shown in Fig.13a, is based on the rigid-body architecture

Table 4 KITE-LS and Wittrick Cross-spring kinetostatic properties

	KITE-LS at ±45°		Cross-spring Wittrick at ±45°	
Mechanical properties	AM	FEM	AM	FEM
Max Von Mises Stress σ_{max} [MPa]	800	902	800	974
Secant stiffness K_θ [Nmm/rad]	214.4	212.3	28	31
Parasitic shift λ [m]	0	134e-6	0	155e-6

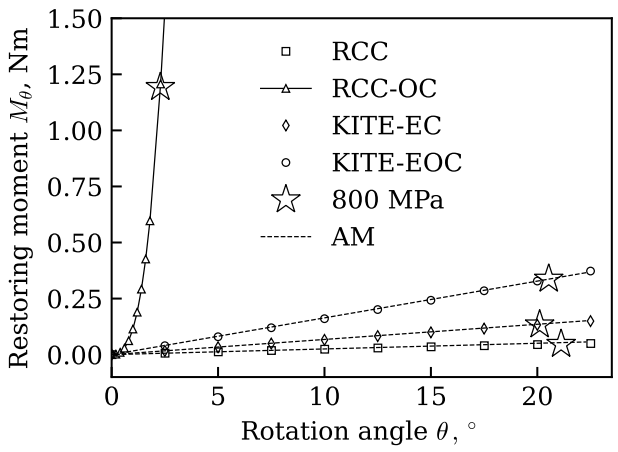

Fig. 11 Elastic restoring moment of KITE-EC (M=1), KITE-EOC (M=-5), RCC (M=1) and RCC-OC (M=-1) pivots. Failure points (800 MPa) from FEM are marked with a star.

presented in Fig. 4. To improve radial stiffness, two additional redundant coupling beams are introduced. The symmetric topology of this pivot provides two significant advantages. First, it enables elimination of the internal degree of freedom of the intermediate stage by introducing a single additional coupling, as shown in Fig. 4b,c. This coupling can be implemented as a compliant connection using a single beam whose function is to enforce a 1:-1 transmission ratio between two opposing base links, as illustrated in Fig. 13c. Ideally, the orientation and length of this beam should follow the guidelines established in [42] to ensure accurate inversion. Second, as observed in Fig. 13, the relative motion of the opposing base links causes them to move toward each other with a second-order displacement when the flexure pivot is rotated. This allows to tune the effective stiffness of the large-stroke flexure pivot over a wide angular range by applying a constant force N on these links, as described in Eq. 13.

4.4.2 Parasitic shift discussion. Interestingly, FEM simulations show that the parasitic motion of the KITE-LS pivot is significantly lower than that of the simple KITE-EC pivot, as shown in Fig. 14. This result is mainly attributed to the symmetrical and serial arrangement of the architecture which compensates for the horizontal (odd-order) component of the parasitic motion of a single KITE-EC. This compensation effect was also observed in the compound Wittrick pivot described in [22]. Moreover, the KITE-LS has systematically lower parasitic motion that the CS-Wittrick pivot, which is the only cross-spring without second-order parasitic shift. Fig. 14 suggests that this improved accuracy stems from the fact that the first-order parasitic motion visible in the CS-Wittrick, arising from the traction-compression of the guiding beams and visible as a linear component of the curve up to approximately 20°, is more pronounced in the cross-spring pivot topology than in the KITE.

4.4.3 Angular stroke and elastic restoring moment validation and discussion. As expected from the previous observations on the KITE-EC, the analytical model underestimates the maximum stress by approximately 10% at a rotation of 45° because of the axial stress in the beams, neglected in the admissible stroke model. The stiffness of the pivot remains remarkably constant over its full angular range, with only a 1% stiffening at ±45° (Tab.4).

4.4.4 Rotational stiffness tuning. Figure 15 shows that the second-order analytical model accurately predicts the stiffness variation of the flexure pivot, allowing a 50% stiffness reduction ($N/N_0 = 0.5$), an almost zero stiffness condition ($N/N_0 = 1$), or even bistable behavior ($N/N_0 = 1.2$). The nonlinear deviations at higher axial loads result from neglecting the axial load's effect on parasitic motion in the analytical model (assumption 2 in C). In practice, this preload can be applied by adding a simple predeformed spring to the KITE-LS, which also provides a convenient stiffness adjustment mechanism, or by using buckled beams, whose reaction force remains nearly constant over displacement (Fig. 13 b,d).

4.4.5 Application perspectives. Overall, this pivot topology enables a large-stroke (±45°) mechanism whose parasitic motion is further reduced compared to the simple KITE-EC pivot. Its internal degree of freedom can be easily eliminated using a single coupling beam, an important consideration for applications where dynamic behavior is critical, such as robotics or systems subject to large vibrations, for instance in space equipment. This pivot can furthermore be tuned toward a near-zero-stiffness configuration, unlocking promising possibilities for high-sensitivity sensor applications [14]. However, for such large range of motion, the load-bearing capacity in the constrained directions is expected to decrease nonlinearly with the rotation angle, a behavior similar to that observed in [20]. This nonlinear support-stiffness loss should be investigated to fully characterize the guiding capacity of this large-angle flexure pivot design.

5 Conclusion

This article introduces a new family of geometrically exact planar remote center of motion (RCM) mechanisms. Exactness is shown to arise from a strict 1:1 transmission condition between links, providing a clear functional interpretation of remote center behavior.

Building upon this kinematic foundation, a transmission-based compliant design methodology is proposed. When implemented as monolithic flexures, these RCM architectures provide versatile solutions for high-precision pivots that are inherently free from backlash and solid friction, while remaining compatible with conventional manufacturing processes and miniaturization. A nonlinear analytical formulation is developed to predict the principal kinetostatic properties of the pivots, including parasitic center-of-rotation (CoR) shift, rotational stiffness, and admissible angular stroke.

The capabilities of the new KITE flexure-based pivot familly are demonstrated through three flexure pivot architectures that push traditional performance limits. The first achieves an exactly constrained planar RCM pivot with zero second-order parasitic motion and nearly constant stiffness. The second introduces an exactly-overconstrained architecture that increases radial and axial stiffness while preserving restoring moment linearity and angular

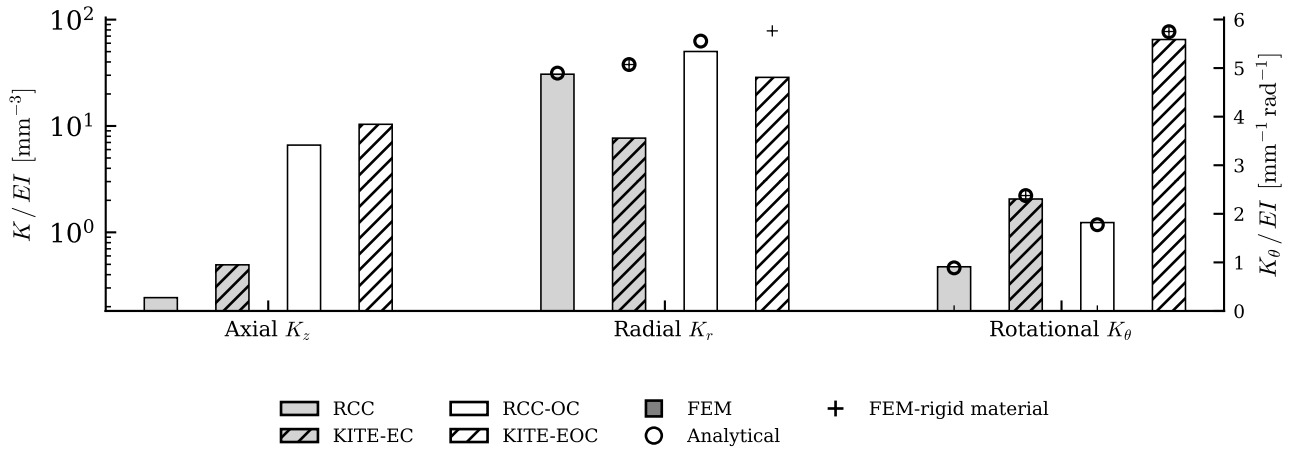

Fig. 12 Translational axial (out-of-plane) stiffness, translational radial stiffness and rotational stiffness of RCC, RCC-OC, KITE-EC and KITE-EOC flexure pivots.

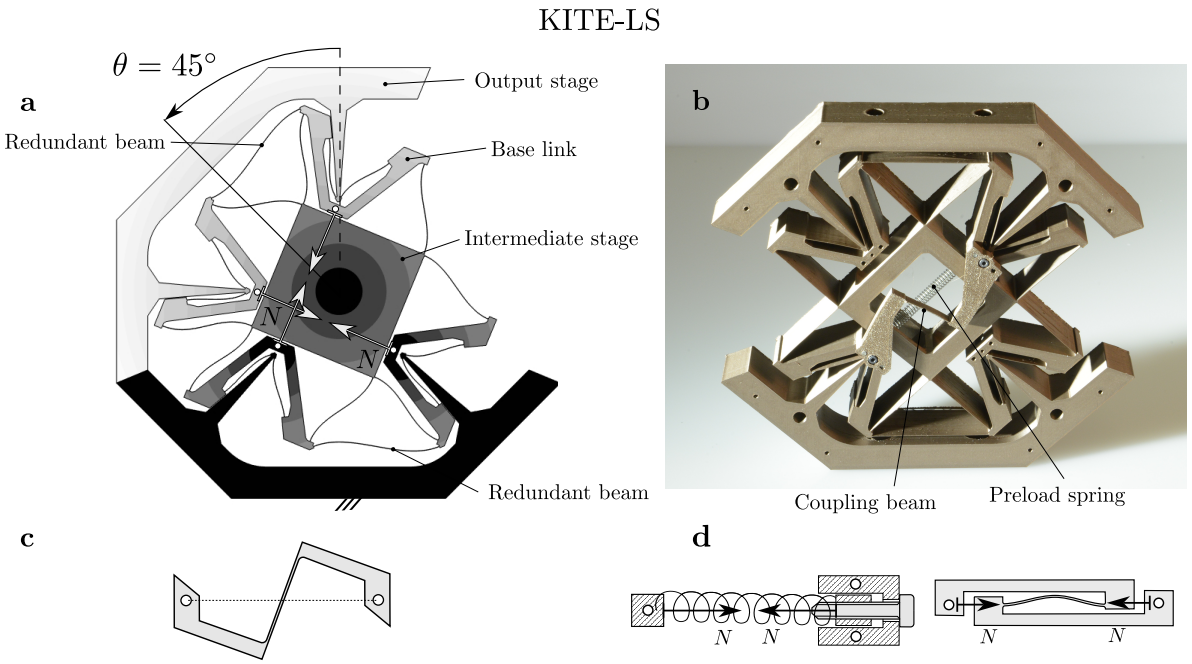

Fig. 13 (a) FEM displacement fields of the large-stroke RCM pivot reaching ±45°. In the configuration shown here two redundant coupling beams are added to improve the radial stifness. (b) 3D printed prototype incorporating a coupling beam and a preload spring. (c) Coupling link connecting two opposing base links to eliminate intermediate-stage internal DoF. (d) Two preload mechanism connecting two opposing base links with an approximately constant force that reduces rotational stiffness.

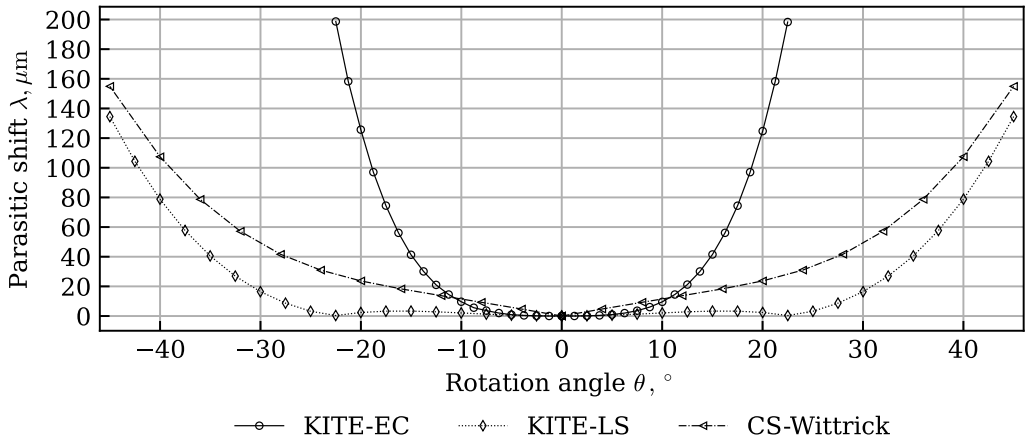

Fig. 14 Parasitic shift from FEM simulations of the exactly-constrained KITE pivot (KITE-EC), the large-stroke KITE pivot (KITE-LS), and the cross-spring pivot with Wittrick's crossing ratio (CS-Wittrick) when an angle θ is applied to the stage.

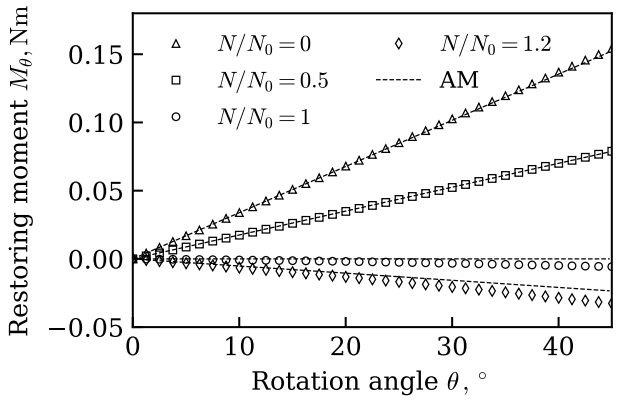

Fig. 15 Reaction moment of the KITE-LS when a constant force *N* is applied on the base links

stroke, thereby overcoming a classical trade-off in flexure pivot design. The third realizes a large-stroke pivot with ±45° rotation and tunable stiffness, extending the attainable motion range of flexure-based pivots.

Future work will focus on experimental validation of the predicted kinetostatic properties, including quantitative measurement of parasitic CoR shift, rotational stiffness, and radial and out-of-plane stiffness. Manufacturing of prototype pivots using wire electrical discharge machining (EDM) is planned. Further investigation will also address a systematic study of the influence of manufacturing tolerances on exactly-overconstrained architectures.

Overall, this work shows that combining kinematic synthesis, nonlinear beam motion modeling, and transmission-oriented design enables the systematic development of high-accuracy, high support stiffness, and large-stroke flexure pivots, advancing the state of the art in compliant RCM pivot mechanisms.

Nomenclature

RCM = Remote Center of Motion
CoR = Center of Rotation
ICR = Instantenous Center of Rotation
RCC = Remote Center of Compliance
DoF = Degree(s) of Freedom
M = Mobility
AM = Analytical Model
FEM = Finite Elements Method

Appendix A: Flexure-based Variants Examples

In this appendix, several flexure-based implementations of the KITE architecture are presented to illustrate the broad design versatility of the pivot family. Figure 16 shows four flexure configurations of:

a: An overconstained version of the *Kite* with 10 overconstraints (4 for added flexure pivots and 6 for added base links homokinetic coupling). This design is well suited for applications demanding ultra-high radial and out-of-plane stiffness.

b: A large-stroke flexure pivot with a single degree of freedom and no internal mobility. This serial arrangement doubles the admissible stroke of the stage relative to that of a single flexure pivot. An additional coupling kinematic made of a flexure inverting link and positioned on a parallel plane, constrains the mechanism to one degree of freedom and prevents undesired excitation of the central connecting body. This coupling also enhances the overall radial stiffness of the flexure pivot.

c: An exactly constrained RCM pivot designed to be actuated by a ±100 μm-stroke linear actuator, resulting in a ±1° angular stroke of the rotating stage. Finite-element simulations predict a parasitic center-of-rotation shift below ±50 nm over the full range of motion after preliminary topology optimization. This design variant, based on the topology shown in Fig. 2**b**, replaces all revolute joints with simple notch hinges, enabling scalable monolithic fabrication from a single metal plate.

d: A monolithic flexure-based 2 DoF tip-tilt stage with orthogonal rotation axis and without parasitic motion made of two serial RCM pivots.

Appendix B: Stiffness, angular stroke and parasitic shift of cross-spring flexure pivot

Figure 17 shows the design of a generic cross-spring privot. remote center of compliance (RCC) flexure pivot.

For a flexure pivot under pure moment, the second order parasitic translation along y of the center of rotation OO' is approximated by the vector $\underline{\lambda}$. Its direction is defined by the bisector of the two beams making up the pivot. The norm of $\underline{\lambda}$ in the y direction follows the second relationship :

$$\lambda_\mathrm{p} = k_\mathrm{p} L \mathrm{p} \theta^2 \tag{B1}$$

The second order constant k is given in [22] :

$$k_p = \frac{9\eta^2 - 9\eta + 1}{15\cos\alpha} \tag{B2}$$

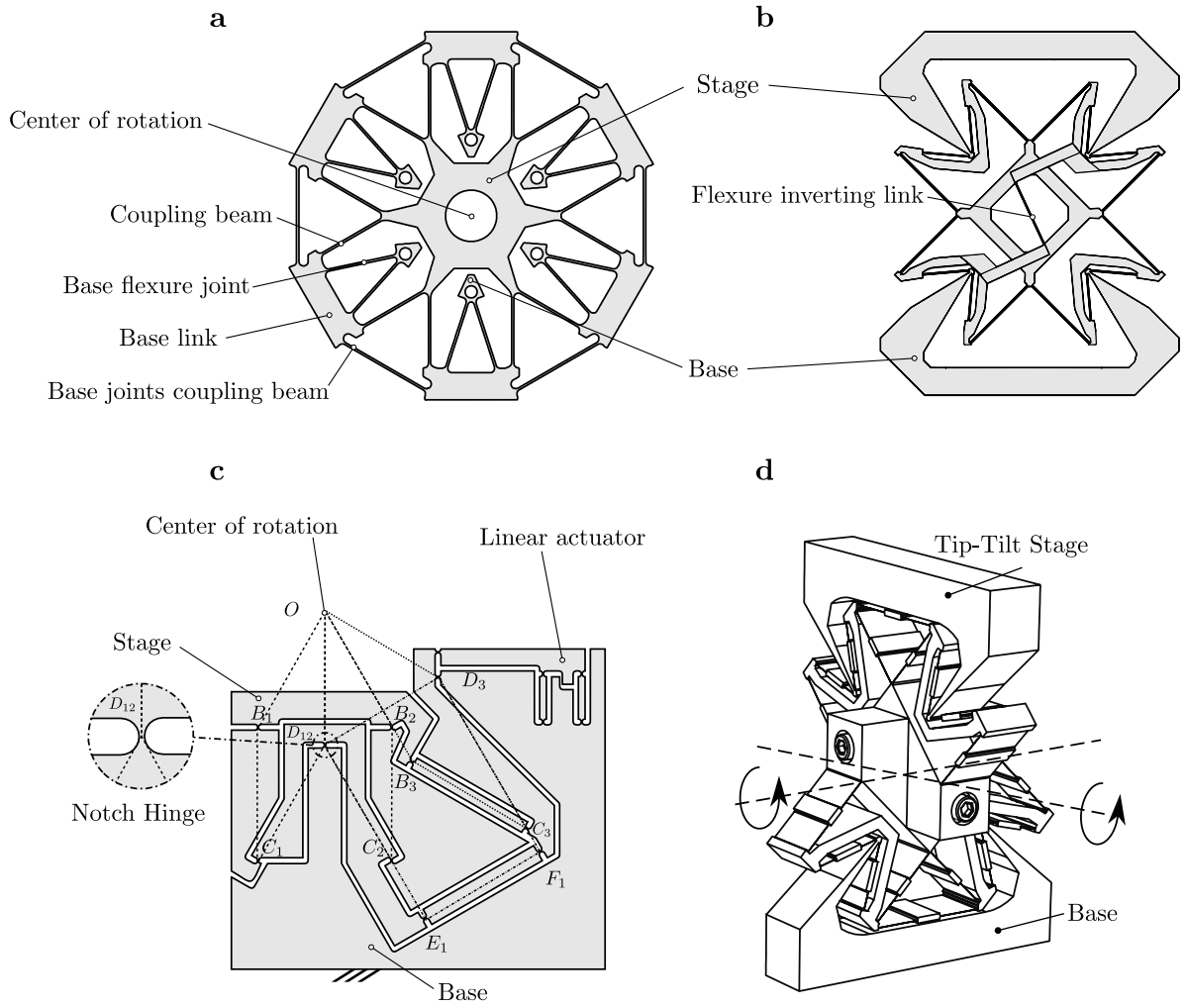

Fig. 16 Flexure implementation of (a): a ten times exactly-overconstrained RCM flexure pivot (Mobility: M=-9); (b): Large-stroke exactly-constrained configuration (Mobility: M=1); (c): A flexure-based RCM pivot embodied with notch hinges and linearly actuated; (d): An exactly constrained 2 DOF flexure-based cardan-joint with concurrent axis and with near-zero parasitic shift.

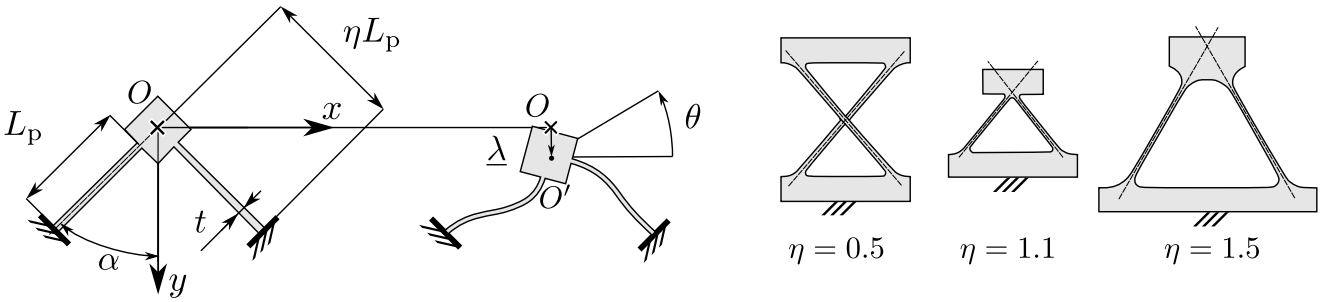

Fig. 17 a, Dimension of a generic cross spring planar flexure pivot. b, Deformed shape of the flexure pivot. For a rotation of θ a second order translation $\underline{\lambda}$ in the direction β is observed.

In the case of a RCC pivot, $\eta > 1$, the cross-spring pivot is fully planar and has a parasitic CoR shift in the direction of the fixed base. But this equation is still valid for $\eta < 1$. As a result, the corresponding cross-spring pivot is built in two distinct parallel planes and can have a negative value for k, meaning that the parasitic displacement tends to move the center of rotation away from the fixed base. For $\eta = 1/2 \pm \sqrt{5}/6$, the cross-spring pivot has no second-order parasitic shift [18].

The angular stiffness of the flexure pivot is:

$$K_{\theta,p} = \frac{8EI}{L_p}(3\eta^2 - 3\eta + 1), \text{ with } I = \frac{bt^3}{12} \tag{B3}$$

With t is the thickness of the leaf springs, b their width, and E the Young's modulus of the material they are made of.

The angular stroke of the flexure pivot is given in [29] :

$$\theta_{adm} = \pm \frac{\sigma_{adm} L_p}{Et(3\eta - 1)} \tag{B4}$$

with σ_{adm} the maximum admissible stress in the beam.

Appendix C: Coupling beam geometric axial shortening

This section introduces the geometric beam model that expresses the shortening of the flexible coupling element, λ_b, as a function of f, L, θ, within the framework of Euler–Bernoulli beam theory. While similar to the BCM model in [45], it modifies the formulation by incorporating different boundary conditions and neglects axial force contributions.

The deflection of the beam is modeled with Euler-Bernoulli beam theory equation :

$$EIv''(u) = -M(u) = -M + P(L - u) \tag{C1}$$

where $v''(u)$ is the second derivative of the beam's deflection, E is the Young's modulus, I the second moment of area of the beam with a constant thickness t. The bending moment $M(u)$ is assumed to vary linearly along u, arising from a constant end moment M and a transverse tip force P acting perpendicular to the neutral axis over a beam of length L. This model neglects axial loads and the resulting strains along the beam's neutral axis, assuming that beam shortening arises primarily from curvature during deformation. From the Euler-Bernoulli beam theory relation in C1, the displacement field of the deformed beam is expressed as a third-order polynomial. :

$$v(u) = b_3u^3 + b_2u^2 + b_1u + b_0 \tag{C2}$$

By imposing the boundary conditions :

$$v(0) = 0, v(L) = f = 0, v'(0) = \theta, v'(L) = \theta \tag{C3}$$

Where the boundary condition $f = 0$ comes from the loop-closure equations in the y direction.

we get :

$$b_0 = 0,\ b_1 = \theta,\ b_2 = \frac{3\theta}{L},\ b_3 = \frac{2\theta}{L^2} \tag{C4}$$

The second order displacement of the beam's tip in the neutral axis direction is found using the classical formula :

$$\lambda b = \frac{1}{2}\int_0^L v'(u)^2 du \tag{C5}$$

Which remains valid under the assumption that $v'(u) << 1$.

By substituting C2 in C5 and using appropriate boundary conditions from C4, we get the beam axial shortening λ_b in function of imposed geometrical boundary condition θ and length L.

$$\lambda_b = \frac{1}{10}L\theta^2 \tag{C6}$$

Appendix D: Cross-spring pivots Dimensions

Tables 5 and 6 list the dimensions of the cross-spring pivots used as reference designs in the FEM comparison. The beam length L_p is determined from Eq. B4 such that the maximum stress does not exceed the admissible limit of 800 MPa.

Table 5 RCC Dimensions

L_p [mm]	t [mm]	b [mm]	η [-]	α [°]	θ_{adm} [°]
38.2	0.1	10	1.65	45	22.5

Table 6 Wittrick Cross-spring pivot Dimensions

L_p [mm]	t [mm]	b [mm]	η [-]	α [°]	θ_{adm} [°]
31.1	0.1	10	$1/2 + \sqrt{5}/6$	45	45

Appendix E: Axial, radial and rotational stiffness of flexure pivots

The Tab. 7 gives the numerical values used to discuss support stiffness of the KITE-EC, KITE-EOC, RCC and RCC-OC in the sections 4.2.4 and 4.3.4. The FEM model corresponds to the case where all pivot components are modeled as linear elastic, whereas the FEM-rigid model assumes rigid connections between the beams. FEM simulations do not includes large-deformation (linear regime), assuming small deformations.

Table 7 Translational and rotational stiffness of the flexure pivots.

Stiffness	Model	RCC	KITE-EC	RCC-OC	KITE-EOC
Axial K_z [N/mm]	FEM	39.73	80.84	1079.87	1694.20
Radial K_r [N/mm]	FEM	5011.78	1256.09	8194.03	4680.33
	AM	5130.89	6178.45	10261.78	—
	FEM rigid	—	6178.56	—	12799.84
Rotational K_θ [Nmm/rad]	FEM	148.61	376.50	297.24	912.69
	AM	145.32	387.97	290.64	939.32
	FEM rigid	—	388.08	—	939.58

References

[1] Zhang, W., Wang, Z., Ma, K., Liu, F., Cheng, P., and Ding, X., 2024, "State of the art in movement around a remote point: a review of remote center of motion in robotics," ENGINEERING Mechanical Engineering, **19**(2), p. 14.

[2] Zong, G., Pei, X., Yu, J., and Bi, S., 2008, "Classification and type synthesis of 1-DOF remote center of motion mechanisms," Mechanism and Machine Theory, **43**(12), pp. 1585–1595.

[3] Taylor, R., Jensen, P., Whitcomb, L., Barnes, A., Kumar, R., Stoianovici, D., Gupta, P., Wang, Z., Dejuan, E., and Kavoussi, L., 1999, "A Steady-Hand Robotic System for Microsurgical Augmentation," The International Journal of Robotics Research, **18**(12), pp. 1201–1210, Publisher: SAGE Publications Ltd STM.

[4] Näf, M. B., Junius, K., Rossini, M., Rodriguez-Guerrero, C., Vanderborght, B., and Lefeber, D., 2018, "Misalignment Compensation for Full Human-Exoskeleton Kinematic Compatibility: State of the Art and Evaluation," Applied Mechanics Reviews, **70**(5), Publisher: American Society of Mechanical Engineers Digital Collection.

[5] Xu, Q., 2015, "Design of a Large-Range Compliant Rotary Micropositioning Stage With Angle and Torque Sensing," IEEE Sensors Journal, **15**(4), pp. 2419–2430.

[6] Tissot-Daguette, L., Baur, C., Bertholds, A., Llosas, P., and Henein, S., 2021, "Design and modelling of a compliant constant-force surgical tool for objective assessment of ossicular chain mobility," *2021 21st International Conference on Solid-State Sensors, Actuators and Microsystems (Transducers)*, IEEE, pp. 1299–1302.

[7] Bittner, H., Erdmann, M., Herdt, B., and Steinacher, A., 1998, "Optical system of the SOFIA Telescope," *Space Telescopes and Instruments V*, Vol. 3356, SPIE, pp. 512–521, doi: 10.1117/12.324474.

[8] Sweeney, M. N., Rynkowski, G. A., Ketabchi, M., and Crowley, R., 2002, "Design considerations for fast-steering mirrors (FSMs)," *Optical Scanning 2002*, Vol. 4773, SPIE, pp. 63–73.

[9] Henein, S., Spanoudakis, P., Schwab, P., KJELBERG, I., Giriens, L., and Dassa, L., 2010, "Flexure-based pointing mechanism with sub-microradian resolution for the Laser Interferometer Space Antenna," .

[10] Bacher, J., Joseph, C., and Clavel, R., 2002, "Flexures for high precision robotics," Industrial Robot: the international journal of robotics research and application, **29**(4), pp. 349–353.

[11] Naves, M., Nijenhuis, M., Seinhorst, B., Hakvoort, W. B. J., and Brouwer, D. M., 2021, "T-Flex: A fully flexure-based large range of motion precision hexapod," Precision Engineering, **72**, pp. 912–928.

[12] Magleby, S., Merriam, E., Jones, J., and Howell, L., 2013, "Monolithic 2 DOF fully compliant space pointing mechanism," Journal of Mechanical Sciences, **4**, pp. 381–390.

[13] Kota, S., Joo, J., Li, Z., Rodgers, S. M., and Sniegowski, J., 2001, "Design of Compliant Mechanisms: Applications to MEMS," Analog Integrated Circuits and Signal Processing, **29**(1), pp. 7–15.

[14] Tissot-Daguette, L., Smreczak, M., Baur, C., and Henein, S., 2021, "Load cell with adjustable stiffness based on a preloaded T-shaped flexure pivot," .

[15] Kahrobaiyan, M. H., Thalmann, E., Rubbert, L., Vardi, I., and Henein, S., 2018, "Gravity-Insensitive Flexure Pivot Oscillators," Journal of Mechanical Design, **140**(075002).

[16] Tissot-Daguette, L., Cosandier, F., Thalmann, E., and Henein, S., 2024, "Near-Zero Parasitic Shift Flexure Pivots Based on Coupled n-RRR Planar Parallel Mechanisms," Journal of Mechanisms and Robotics, **16**(111006).

[17] Thalmann, E., Kahrobaiyan, M. H., Vardi, I., and Henein, S., 2019, "Flexure Pivot Oscillator With Intrinsically Tuned Isochronism," Journal of Mechanical Design, **142**(075001).

[18] Wittrick, W. H., 1951, "The properties of crossed flexure pivots, and the influence of the point at which the strips cross," Aeronautical Quarterly, **2**(4), pp. 272–292.

[19] Thalmann, E. and Henein, S., 2022, "Triple Crossed Flexure Pivot Based on a Zero Parasitic Center Shift Kinematic Design," Journal of Mechanisms and Robotics, **14**(045001).

[20] Spanoudakis, P., Kiener, L., Cosandier, F., Schwab, P., Giriens, L., Kruis, J., Grivon, D., Psoni, G., Vrettos, C., and Bencheikh, N., 2019, "Large angle flexure pivot development for future science payloads for space applications," MATEC Web of Conferences, **304**, p. 07016, Publisher: EDP Sciences.

[21] Liu, T., Bi, S., Yao, Y., Dong, Z., Yang, Q., and Liu, L., 2020, "Research on zero-stiffness flexure hinge (ZSFH) based on spring four-bar linkage(4BSL)," Mechanism and Machine Theory, **143**, p. 103633.

[22] Hongzhe, Z. and Shusheng, B., 2010, "Accuracy characteristics of the generalized cross-spring pivot," Mechanism and Machine Theory, **45**(10), pp. 1434–1448.

[23] Qu, J., Chen, W., Zhang, J., and Chen, W., 2016, "A large-range compliant micropositioning stage with remote-center-of-motion characteristic for parallel alignment," Microsystem Technologies, **22**(4), pp. 777–789.

[24] Pieber, M. and Gerstmayr, J., 2023, "Six-Bar Linkages With Compliant Mechanisms for Programmable Mechanical Structures," Journal of Mechanisms and Robotics, **16**(061008).

[25] Henein, S., Spanoudakis, P., Schwab, P., KJELBERG, I., Giriens, L., Welte, Y., Dassa, L., Greger, R., and Langer, U., 2009, "DESIGN AND DEVELOPMENT OF THE POINT-AHEAD ANGLE MECHANISM FOR THE LASER INTERFEROMETER SPACE ANTENNA (LISA)," .

[26] Hartig, M.-S., Schuster, S., and Wanner, G., 2022, "Geometric tilt-to-length coupling in precision interferometry: mechanisms and analytical descriptions," Journal of Optics, **24**(6), p. 065601, Publisher: IOP Publishing.

[27] 1998, "Trefoil Rotary Flexure," https://saemobilus.sae.org/articles/trefoil-rotary-flexure-tbmg-32044, Accessed: 2025-11-13.

[28] Yao, Y., Bi, S., and Zhao, H., 2012, "Analytical Modeling and Analysis of an Annulus-Shaped Flexural Pivot," *Volume 4: 36th Mechanisms and Robotics Conference, Parts A and B*, American Society of Mechanical Engineers, Chicago, Illinois, USA, pp. 259–265, doi: 10.1115/DETC2012-70592.

[29] Cosandier, F., Henein, S., Richard, M., and Rubbert, L., 2017, *The Art of Flexure Mechanism Design*, EPFL Press.

[30] Liu, L., Bi, S., and Yang, Q., 2018, "Stiffness characteristics of inner–outer ring flexure pivots applied to the ultra-precision instruments," Proceedings of the Institution of Mechanical Engineers, Part C: Journal of Mechanical Engineering Science, **232**(13), pp. 2441–2457, Publisher: IMECHE.

[31] Bai, R., Zhang, H., Yang, N., Yu, Z., Li, B., Xu, Q., and Chen, G., 2025, "Optimization of a near-zero-center-shift compliant pivot for large motion range and high bearing stiffness," Mechanism and Machine Theory, **216**, p. 106218.

[32] Pechhacker, A., Palka, C., Csencsics, E., and Schitter, G., 2026, "Hybrid reluctance actuator topology for enhanced linearity and high torque in fast steering mirrors," Precision Engineering, **97**, pp. 16–23.

[33] Di, D. G., Hinaux, B., Klinger, L., and Helfer, J.-L., 2016, "Timepiece Resonator with Crossed Blades," .

[34] Shi, Z., Liu, Y., Zhao, Z., Wang, Z., Yan, Y., Fan, L., Li, Z., and Zhao, H., 2023, "Design and analysis of ultra-low moment noise flexure pivot in space gravitational wave detectors," Classical and Quantum Gravity, **40**(20), p. 205016, Publisher: IOP Publishing.

[35] Huo, T., Yu, J., Zhao, H., Wu, H., and Zhang, Y., 2021, "A family of novel RCM rotational compliant mechanisms based on parasitic motion compensation," Mechanism and Machine Theory, **156**, p. 104168.

[36] Zhang, Z., Pieber, M., and Gerstmayr, J., 2025, "Generalized optimization approach to design in-plane distributed compliant remote center of motion mechanism," Mechanism and Machine Theory, **205**, p. 105890.

[37] Henein, S., Spanoudakis, P., Droz, S., Myklebust, L. I., and Onillon, E., 2003, "FLEXURE PIVOT FOR AEROSPACE MECHANISMS," th European Space Mechanisms and Tribology Symposium.

[38] Pei, X., Yu, J., Zong, G., Bi, S., and Hu, Y., 2009, "A Novel Family of Leaf-Type Compliant Joints: Combination of Two Isosceles-Trapezoidal Flexural Pivots," Journal of Mechanisms and Robotics, **1**(021005).

[39] Fowler, R. M., Maselli, A., Pluimers, P., Magleby, S. P., and Howell, L. L., 2014, "Flex-16: A large-displacement monolithic compliant rotational hinge," Mechanism and Machine Theory, **82**, pp. 203–217.

[40] Smith, S. T., 2017, *Foundations of Ultra-Precision Mechanism Design*, CRC Press, London.

[41] Bai, R., Ma, F., Li, B., and Chen, G., 2025, "Design a Compliant Pivot with Nearly Zero Axial Drift and High Radial Stiffness," *Advances in Mechanism and Machine Science and Engineering in China*, Y. Chen, L. Liu, X. Liu, H. Liu, M. Li, and T. Sun, eds., Springer Nature, Singapore, pp. 3–14, doi: 10.1007/978-981-96-1464-6_1.

[42] Vallat, C., Tissot-Daguette, L., Cosandier, F., and Henein, S., 2026, "Optimized design of generalized flexure rotational couplers," Precision Engineering, **97**, pp. 961–976.

[43] Hubbard, N. B., Wittwer, J. W., Kennedy, J. A., Wilcox, D. L., and Howell, L. L., 2008, "A Novel Fully Compliant Planar Linear-Motion Mechanism," American Society of Mechanical Engineers Digital Collection, pp. 1–5, doi: 10.1115/DETC2004-57008.

[44] Wu, Y., Hai, H., Fang, S., Fan, W., Song, J., Zhao, K., Zhang, R., He, B., Zhao, H., Li, Z., Fan, L., and Yan, Y., 2023, "A fast steering mirror with ultra-low geometric tilt-to-length coupling noise for space-borne gravitational wave detection," Measurement Science and Technology, **35**(1), p. 015407, Publisher: IOP Publishing.

[45] Awtar, S., Slocum, A. H., and Sevincer, E., 2006, "Characteristics of Beam-Based Flexure Modules," Journal of Mechanical Design, **129**(6), pp. 625–639.